JOURNAL OF AIRCRAFT
Vol. 47, No. 2, March–April 2010

Mean Flowfield Structure of a Supersonic Three-Dimensional Base Flow

Datta V. Gaitonde*
U.S. Air Force Research Laboratory, Wright–Patterson Air Force Base, Ohio 45433

DOI: 10.2514/1.45144

The mean flowfield structure in the wake region of a circular cylinder at a 10 deg angle of attack in a Mach 2.5 flow is described. Results from the full three-dimensional Reynolds-averaged Navier–Stokes equations, supplemented with a compressibility-corrected two-equation turbulence model, are compared with extensive available experimental data. Mesh resolved results indicate that surface pressure trends on both the afterbody and the base are reproduced well, but quantitative differences of about 15% are observed in different regions. The main experimental observations of the shock pattern, surface oil flow on the afterbody and the base surfaces, velocity vector plots in the symmetry and lateral planes, and end-view flow images are reproduced to good accuracy. Based on this success, the computed solution is employed to generate a model for the mean flow. The main feature is a pair of longitudinal vortices separated by high-speed fluid entrained primarily from the leeward and lateral afterbody boundary layers and bounded from below by the windward afterbody boundary layer. The mean vorticity distribution reveals a vortex core pair forming a horseshoelike structure. The three-dimensional wave structure is elucidated and correlated with the streamline pattern.

I. Introduction

THE drag associated with the flow downstream of a slender body in supersonic flight can be a significant factor in the aerodynamics encountered during its trajectory. Of the three main components of drag, that is, base, wave, and skin friction, the first dominates at supersonic speeds. A comprehensive review of base drag and heat transfer for different canonical shapes and their correlation to key flow parameters has been provided in [1].

Most studies of base flows have focused on zero-degree-angle-of-attack situations. The key features of the mean flow encountered are shown in Fig. 1, reproduced with permission from [1], which shows the region on only one side of the axis of symmetry. The boundary layer developing along the surface undergoes a rapid expansion, followed by a lip shock wave. A recirculating region is evident downstream of the base. Two off-surface stagnation points appear, one where the dividing line meets the axis ("wake stagnation point") and the second representing the trace of an axisymmetric stagnation line. The flow downstream aligns itself parallel to the axis through a series of shock waves, giving rise to the wake neck.

For axisymmetric situations, several experimental and computational efforts have explored details of the turbulent wake region without the complications associated with stings. In the experimental category are the numerous studies employed to develop correlations in [1] and flight tests such as Fire II [2] (which also include angle-of-attack data) on an Apollo-shaped vehicle. Recent ground tests include the stingless configuration described by Herrin and Dutton [3,4] and Bourdon and Dutton [5], who deployed advanced quantitative and qualitative diagnostics to report highly detailed measurements of the mean and fluctuating fields.

Numerous simulations have also been reported on axisymmetric base flows, with turbulence models ranging in complexity to include algebraic, two-equation, Reynolds stress, and large-eddy simulation models. Forsythe et al. [6] offered a detailed review of computational studies, including those that have attempted to characterize and enhance turbulence modeling accuracy. The data of Dutton et al. have been especially popular for validation purposes in such recent efforts [6–9]. Studies have also focused on the impact of Reynolds number [10] and thermochemical nonequilibrium [11]. At high Reynolds numbers, the dynamics of the base region is known to be dependent principally on the Mach number [1]. The effect of Mach number variation on the dynamics has been analyzed by Kawai and Fujii [12], who identified different mechanisms at work in various speed regimes, as well as peculiarities of the transonic regime.

Although axisymmetric cases have been examined extensively, there are relatively fewer studies of base flows at angle of attack. In addition to those employed to develop correlations [1], experiments have been described by Oberkampf and Bartel [13], who employed velocities and pressures to infer wake dynamics through the interaction of body vortices. More recently, Boswell and Dutton [14,15] and Kastengren and Dutton [16] have provided crucial and interesting results on the effect of three dimensionality in supersonic flight. In addition to the observation of lobed structures in the wake of an afterbody inclined at a 10 deg angle of attack, they noted that the low-velocity region near the base shrinks considerably over the axisymmetric situation and that the base pressure is approximately halved. This latter result is consistent with the angle-of-attack analysis of numerous experimental data presented in [1] and has obvious implications on the aerodynamics of maneuvering projectiles.

Fundamental computational analyses of 3-D supersonic base flows, that is, at angle of attack, are relatively rare. Recent efforts, such as [17,18], have explored nonaxisymmetric shapes stressing practical aspects such as lift, drag, and static and dynamic aerodynamic coefficients. Other noteworthy efforts include those of Sahu [19,20], who examined projectiles at angle of attack, and Himeno et al. [21], who analyzed an incompressible situation.

The present effort seeks to develop a flowfield model for the base flow downstream of a cylinder placed at angle of attack. This is accomplished in two steps. First, the ability of the Reynolds-averaged Navier–Stokes (RANS) equations, closed with a two-equation model, is baselined, with emphasis on mean flowfield prediction. Extensive comparisons with surface and off-surface experimental data, including end-view visualizations, are employed for this purpose. Following the successful conclusion of this goal, the second phase employs the simulations to build a three-dimensional flow model, emphasizing the wave, streamline, and vorticity structures and their interrelationships. The RANS approach does not provide information on unsteady aspects such as turbulent structures in the afterbody boundary layer or shear layer instabilities in the wake

Presented as Paper 573 at the 46th AIAA Aerospace Sciences Meeting and Exhibit, Reno, NV, 7–10 January 2008; received 27 April 2009; revision received 13 August 2009; accepted for publication 24 September 2009.

*Technical Area Leader, High-Speed Flows, Air Vehicles Directorate. Fellow AIAA.

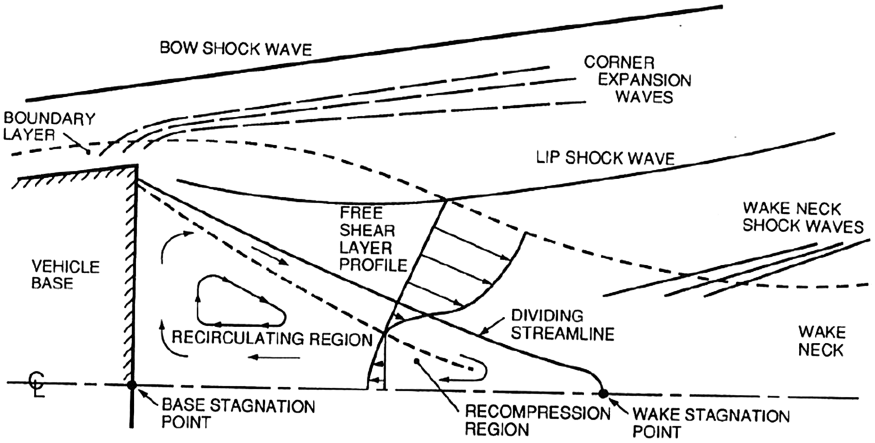

Fig. 1 Schematic of axisymmetric base flow features (figure and permission from Lamb and Oberkampf [1]).

region. However, its ability to provide insight into mean flows, based on a comparison with the experimental data, has been documented in many complex 3-D interactions (see [22–24]).

II. Governing Equations and Numerical Model

The principal elements of the governing equations and numerical model have been provided in numerous references and only a summary is provided here for brevity (see [25]) The unsteady nondimensionalized three-dimensional compressible Reynolds-averaged Navier–Stokes equations in mass-averaged variables are solved in curvilinear coordinates [26]. Nondimensionalization is accomplished with U_∞ for velocity, a boundary-layer height δ, freestream density ρ_∞, and $\rho_\infty U_\infty^2$ for pressure. The effects of turbulence are incorporated by replacing the molecular viscosity μ by the sum, $\mu + \mu_t$, where μ_t is the eddy viscosity and a turbulent Prandtl number ($Pr_t = 0.9$) is introduced in the standard fashion. The baseline two-equation k–ϵ model including low Reynolds number terms employs the work of several authors [27,28] and details of its implementation are given by Rizzetta [29]. The compressibility correction factor is particularly significant for supersonic separated flows such as the one under consideration; for this purpose the approach of Sarkar et al. [28] is employed.

The inviscid fluxes in both the flow and k–ϵ equations are evaluated with the Roe [30] scheme, using the monotone upstream-centered schemes for conservation laws reconstruction procedure [31] to obtain up to nominal third-order accuracy. In the presence of shocks, a limiter is required to stabilize the calculations and enforce monotonicity; in the present work, the van Albada limiter [32] is employed. Viscous and turbulence model source terms are evaluated to second-order accuracy. To facilitate the possible evolution of unsteady solutions, time integration is accomplished with a Beam–Warming approximately factored approach [33] with the efficiency and time-accuracy improvements of the diagonalized formulation [26] and subiterative strategy, respectively, as described in [34].

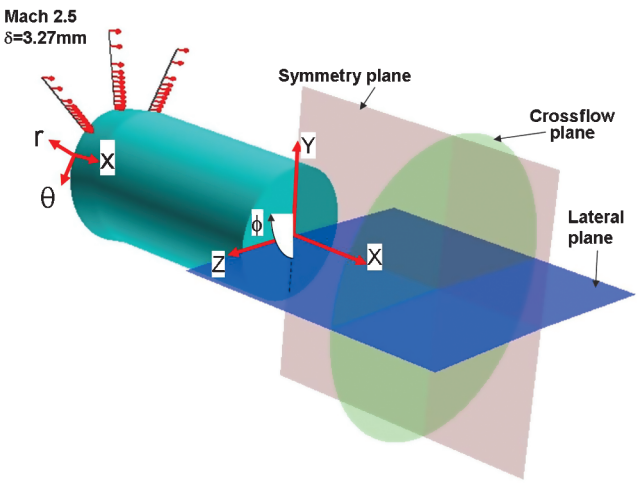

Fig. 2 Schematic of configuration showing coordinate systems.

III. Results

The configuration examined is the flow past a front-mounted afterbody at angle of attack, as shown in Fig. 2, patterned after the experiments in [14–16]. A cylinder of radius $R = 31.75$ mm, with the axis parallel to the flow direction, is effectively bent at a 10 deg angle, yielding a cylindrical afterbody of length L, where $L/R = 3$. The nominal freestream Mach number is 2.45, the stagnation temperature is 300 K, the stagnation pressure is $P_o = 565$ kPa, and the Reynolds number is $Re = 56 \times 10^6$/m. The discussion employs several coordinates as shown in Fig. 2. In the upstream axisymmetric region, x is aligned with the freestream, r is radial, and θ is azimuthal. In the afterbody and base regions, the X coordinate runs normal to the base, that is, at a 10 deg inclination to the freestream; Y points vertical such that X–Y is the plane of symmetry; and Z points spanwise. Following the experimentalists, an azimuthal angle, ϕ, is also employed in the base region. This is measured from the windward side ($\phi = 0$) to the leeward side ($\phi = 180$ deg), traversing counterclockwise when looking downstream. Several results will be plotted on the symmetry ($\phi = 0$, 180 deg), lateral ($\phi = 90$, 270 deg), and crossflow (Fig. 2) planes as marked. All experimental results employed in this paper have been scanned or digitized from [14,15].

A. Inflow Boundary Condition

The inflow boundary condition is specified by matching the boundary layer upstream of the bend to that reported by the experimentalists in [15]. In addition to a boundary-layer height of $\delta_{\exp}/R = 0.103 \pm 1.5\%$ or $\delta_{\exp} = 3.27$ mm, the Sun and Childs [35] formula curve fits were employed to obtain a displacement thickness of $\delta^*_{\exp}/R = 0.0308 \pm 6.4\%$, a momentum thickness of $\theta_{\exp}/R = 0.0081 \pm 5.6\%$, and skin friction coefficient of $C_f = 1.26 \times 10^{-3} \pm 4.4\%$. To generate an equilibrium boundary-layer profile with these properties, a separate axisymmetric calculation was performed of flow past a cylinder of the same radius as the body under examination. The structure of the grid employed, shown in Fig. 3a, consists of an axisymmetric slice discretized by two meshes (denoted A1 and A2) of varying concentration in each of the streamwise, body-normal, and azimuthal directions. The parameters of each mesh are presented in Table 1. The boundary conditions employed for this precursor calculation include a fixed incoming freestream inflow to match the experimentally reported values and zero gradients at the downstream boundary. No-slip and zero pressure gradient conditions are employed at the wall, with either a fixed wall temperature or adiabatic condition (to explore the effect of wall temperature on boundary-layer development). Inviscid wall conditions are applied

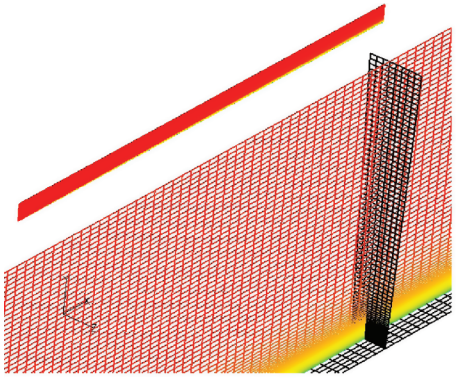

a) Grid structure

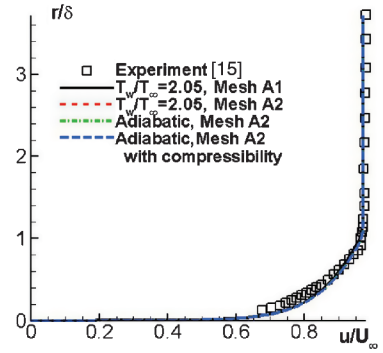

b) Linear scale

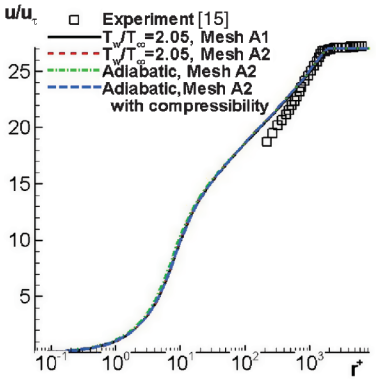

c) Log-linear scale

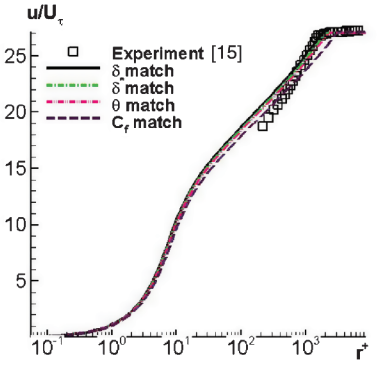

d) Results with different matching criteria

Fig. 3 Normalized velocity profiles matching boundary-layer thickness δ with experiment.

on the azimuthal boundaries, whereas the far field is treated with a nonreflecting condition as described in [36].

Results comparing the computed equilibrium boundary layer with the experiment for the same boundary-layer height are shown in Figs. 3b and 3c in terms of linear and law-of-the-wall coordinates, respectively. Several simulations are shown for the adiabatic and fixed wall temperature (which is derived from other parameters published in [15]), as well as the effect of the compressibility correction, which is not suited for the upstream attached boundary layer but is crucial in the base region characterized by free shear layer interactions. All simulations show very similar profiles, indicating that the simulation is well resolved. When the boundary-layer height is matched, minor variations in wall temperature and the use of a compressibility correction yield no significant variation, and all computed profiles collapse on a single line. However, the comparison with the experiment indicates that the computation has a fuller profile and a different slope on the log plot. Indeed, when δ is matched, the skin friction coefficient varies substantially between computation and experiment: matching $\delta/R = 0.103$ leads to 10% overprediction in C_f relative to the experiment, and 11 and 16% with the incompressible and compressible momentum thicknesses, respectively. Figure 3d plots the experimental values with computed boundary-layer profiles matching the experimental boundary-layer height, δ, the displacement thickness height, δ^*, momentum thickness, θ, and skin friction coefficient, C_f, respectively. On this scale, a C_f match exhibits the largest discrepancies.

Several previous efforts addressing the corresponding axisymmetric experiments have noted similar problems matching the experimental profile with simulations assuming equilibrium boundary-layer development. For example, Forsythe et al. [6] also noted the slightly fuller computational profile. Attempts to factor the nozzle geometry have also been reported: Baurle et al. [7] did not detect improvements, but de Feo and Shaw [8] concluded that accurate simulation of the entire facility, together with an iteratively converged Reynolds stress model, yielded accurate results. In the present work, because a principal boundary length scale entering the interaction is the boundary-layer height, this was chosen as the matching parameter. Thus, the adiabatic simulation on mesh M2, with compressibility correction, was employed to generate the entire axisymmetric incoming boundary layer at the upstream edge of the domain (shown in Fig. 2) through azimuthal extension.

Table 1 Properties of meshes employed for precalculation of incoming boundary layer

Mesh	Points	$\Delta x/\delta$	r^+	$\Delta\theta$
A1	$651 \times 97 \times 5$	0.5	0.09	1°
A2	$1411 \times 151 \times 9$	0.23	0.05	0.5°

B. Three-Dimensional Base Flow: Numerical Aspects

A structured, multiblock mesh is generated for the 3-D region shown in Fig. 2. Some of the main features are shown in Fig. 4. In the structured mesh approach employed, points within the body are blanked. To prevent an excessive number of blanked points, the simulations are conducted sequentially in two domains. The first domain starts 6δ upstream of the bend (measured from the windward side of the juncture) and extends the length of the afterbody. The second domain starts upstream of the base, overlapping with the afterbody simulation, which provides an upstream condition, and extends far downstream. In this second domain, the cylindrical mesh is extended to the axis, yielding a singularity. In this manner, only the second domain has blanked points. Several overlap sizes were investigated: the upstream influence of the corner was found to be negligible in the present RANS approach. The results below employ an overlap region of 8δ.

Various meshes were employed in both domains: the afterbody meshes are denoted B1, B2, and B3, whereas those for the base region are C1, C2, and C3. The grid is composed of streamwise-stacked cylindrical planes ($\xi =$ constant), with a singularity originating at the base center (second domain) and clustered on

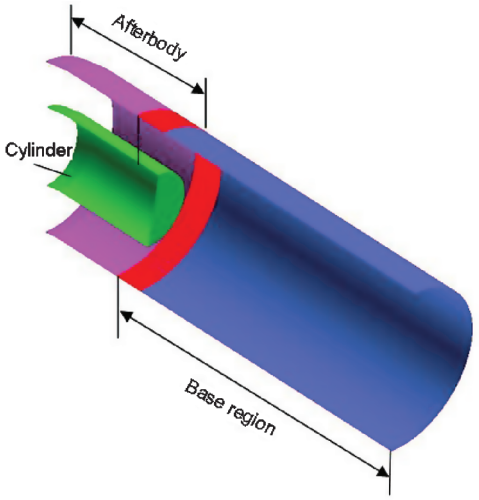

a) Domain decomposition

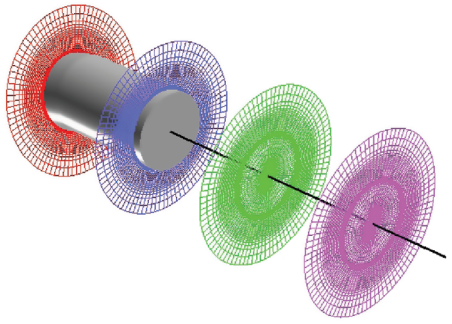

b) ξ planes

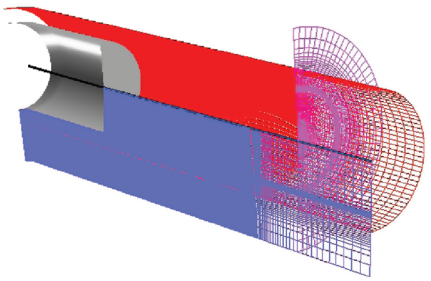

c) ξ planes (reflected about symmetry plane)

Fig. 4 Grid structure and computation strategy of base flow.

solid surfaces and at the singularity, as shown in Fig. 4a. Thus, η planes are cylindrical whereas ζ planes correspond to $\phi =$ constant coordinate surfaces. Details of these meshes are provided in Table 2. In all cases, only one side of the plane of symmetry is computed, except for mesh C3, which has the same number of points as mesh C1, but computes both sides of the symmetry plane. This facilitates detection of possible asymmetric solutions in the instantaneous sense and also permits examination of mesh sensitivity to ζ-mesh resolution.

Table 2 Meshes employed for afterbody and base regions

Mesh	Domain	$IL \times JL \times KL$
B1	Afterbody	$144 \times 88 \times 185$
B2	Afterbody	$144 \times 176 \times 185$
B3	Afterbody	$217 \times 176 \times 275$
C1	Base	$272 \times 276 \times 185$
C2	Base	$272 \times 376 \times 185$
C3	Base (both sides)	$272 \times 276 \times 185$

The domain size is determined by examining the shock and expansion structure of the 3-D flowfield on very coarse meshes (not shown). Based on these, the downstream plane extends 109δ from the base. The outer boundary is placed at a radial distance of 20δ from the surface. This domain size compares favorably with that employed in [7] except in the radial direction, where the present effort has a tighter extent.

At the upstream boundary, the incoming boundary-layer profile is specified to match the boundary-layer thickness on the cylinder surface as described above (afterbody domain) or is derived from the afterbody for the base domain. At the downstream boundary, the flow is entirely supersonic, and a simple zero gradient condition is employed. Nonreflecting boundary conditions are applied in the radial far field, whereas standard wall conditions are enforced on surfaces. The axial singularity in the base domain is treated as a boundary condition by averaging the values at surrounding nodes. Postcomputation analyses indicate that, with the clustering employed near the axis, the solution exhibits discrete continuity across this boundary. When plotting results, both domains are combined into one composite database.

C. Wave Structure

Figure 5 compares the experimental and computed wave structure on the symmetry plane. Figure 5a, taken from [15], exhibits a composite schlieren picture, whereas Fig. 5b exhibits the computed solution with the magnitude of the density gradient ($|\nabla\rho|$).

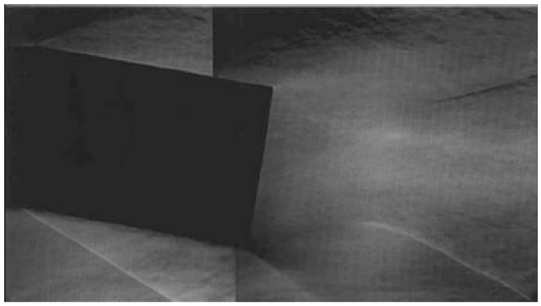

a) Experiment - Schlieren. From [15] with permission

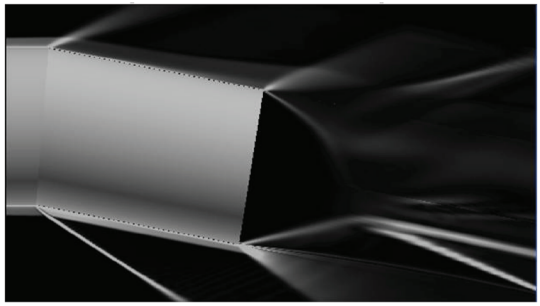

b) Simulation $|\vec{\nabla}\rho|$

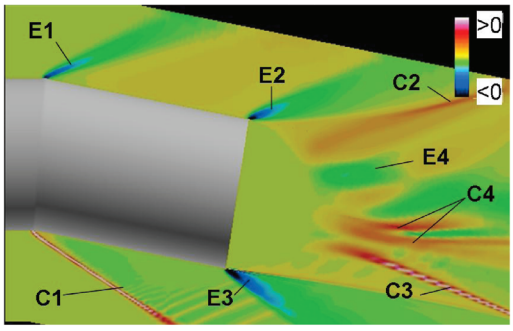

c) Simulation $\vec{v} \cdot \vec{\nabla}p$

Fig. 5 Wave structure on symmetry plane.

Numerous features are readily apparent in each, and to further identify and discuss specific structures, Fig. 5c exhibits the quantity, $\mathbf{V} \cdot \nabla p$, $\mathbf{V} = \{u, v, w\}$, that is, the component of pressure gradient along the velocity vector. This quantity distinguishes between shocks/compressions from expansions. At the former, $\mathbf{V} \cdot \nabla p > 0$, whereas at the latter, $\mathbf{V} \cdot \nabla p < 0$. The main features are marked in Fig. 5c as C (compressions/shocks) and E (expansions). The expansion E1, associated with the bend on the leeward side, and the shock C1, associated with the windward flow, are clearly visible in the experiment and computation, as are the expansions (E2 and E3) associated with the rapid turn at the shoulder. Note that, in three dimensions, these are continuous features, as will be evident in subsequent figures. Similarly, the recompression shocks C2 and C3 are also reproduced in the experiment (Fig. 5a) and computation (Fig. 5b). Detailed scrutiny of the computed feature C2 suggests that the structure originates as a lip shock (see Fig. 1) followed by a compression fan as the flow from the leeward side recovers downstream of the base; this is discussed further in Secs. III.G and III.H in the context of the streamline pattern. Similarly, the feature C3 appears as the equivalent of C2, though stronger, on the windward side. The compression downstream of the shoulder is sharper on this side compared with the leeward, and the lip shock appears relatively distinct from the main segment of C3. The vertical width of the interaction is slightly larger in the computation than in the experiment. However, part of the distinction stems from the only approximately similar scaling between the two figures.

A significant difference between the computation and experiment is the feature marked C4, which is not evident in the experiment. As described in further detail in Sec. III.F, this feature can be correlated with other elements inferred from experimental observations. Between C2 and C4, a sequence of mild expansion (E4) and compression (not marked) is observed. With regard to the boundary-layer growth on the afterbody, both the experiment and simulation show the increase in height of the boundary layer on the lee side, with no evidence of separation. On the windward side, the simulations (Fig. 5b) show that the boundary layer thins after recovering from the effect of the windward shock, C1, as a consequence of increased density and spanwise relief. On this side also, no evidence of separation is observed in either the experiment or computation in this relatively weak interaction.

A similar comparison with the experiment on the lateral plane is depicted in Fig. 6. In this plane, the structure is qualitatively similar to that observed for axisymmetric flows. Figure 6a represents a composite Mie-scattering image from [15]. A key feature observed is the presence of a bright region near the center, described in [15] as warm fluid composed of "entrained lee-side freestream fluid along the flow centerline." The computational result, Fig. 6b, employs the vertical velocity (in the direction of Y) to depict an equivalent. The bright central region is evident in the computation, though size discrepancies are difficult to ascertain because of the difficulty in plotting a quantity precisely equivalent to the Mie-scattering image in terms of brightness. Figure 6c exhibits $\mathbf{V} \cdot \nabla p$ values, on which are marked the identities of the various features observed earlier on the symmetry plane. For example, a wake neck structure is observed, similar to that in Fig. 1. The notation in Fig. 6c highlights the fact that the features are continuous. Thus, expansions E2 and E3 are the traces of the circumferential expansion emanating from the shoulder. Similarly C2 and C3 represent the trace of the recompression system on the lateral plane. A comparison of Fig. 6c with Figs. 6a and 6b indicates that the structure denoted C4 arises due to the sharp gradients between the bright and dark regions. In conjunction with the observations of Fig. 5, C4 is a relatively small annular feature, described in greater detail in Sec. III.F.

The three-dimensional wave structure correlating the observations on the symmetry and lateral planes is depicted in Fig. 7. Figure 7a shows $\mathbf{V} \cdot \nabla p$ on several crossflow planes and the symmetry plane. Each feature is essentially continuous. Note on the first crossflow

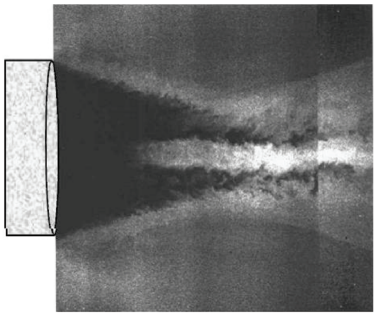

a) Experiment [15] - Mie scattering

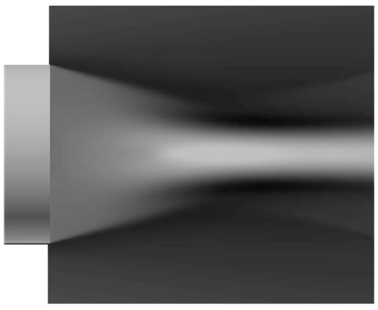

b) Simulation - v field

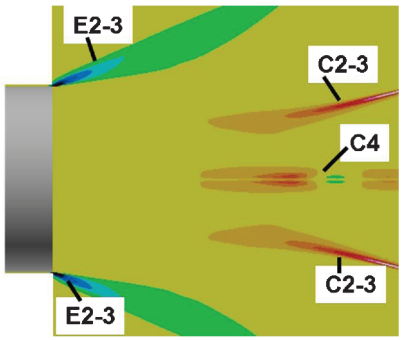

c) Simulation $\vec{V} \cdot \vec{\nabla} p$

Fig. 6 Wave structure on lateral plane.

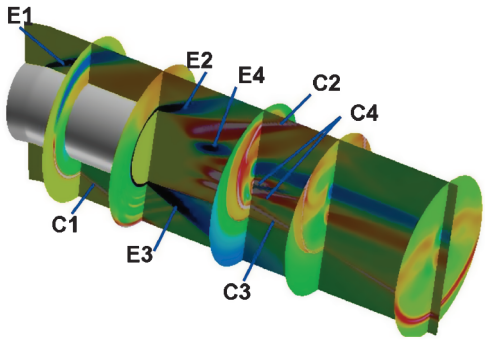

a) Crossflow planes - $\vec{V} \cdot \vec{\nabla} p$

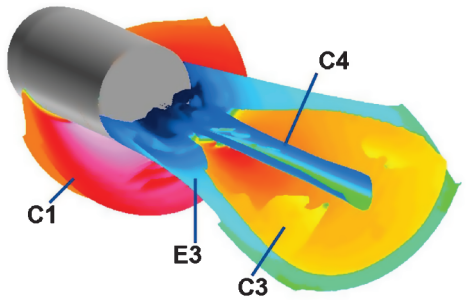

b) Isosurfaces of $\vec{V} \cdot \vec{\nabla} p$ colored by pressure

Fig. 7 Three-dimensional views of composite flow structure.

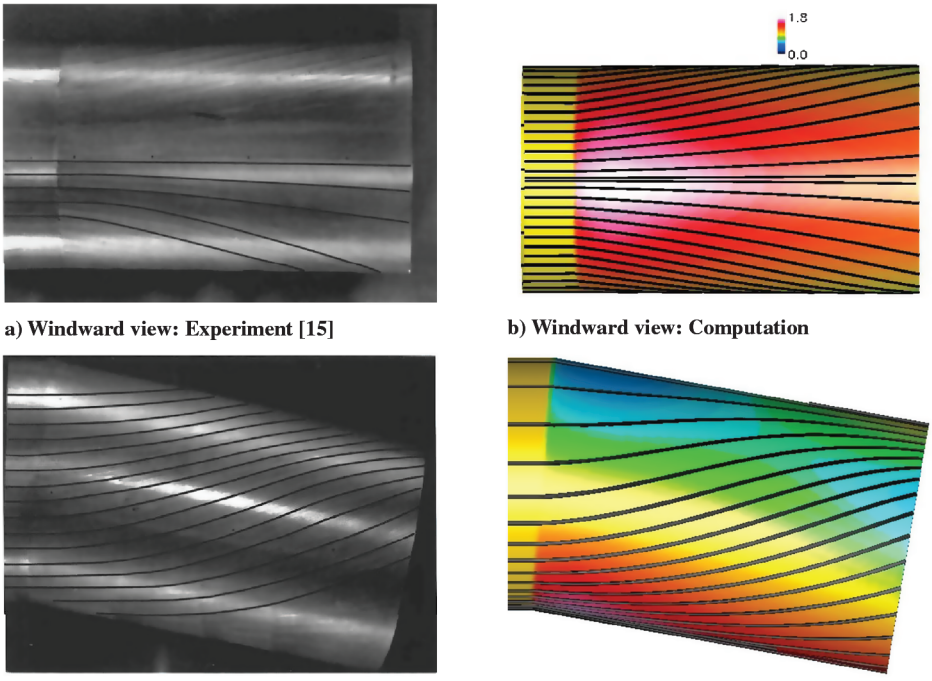

a) Windward view: Experiment [15]

b) Windward view: Computation

c) Side view: Experiment [15]

d) Side view: Computation

Fig. 8 Surface oil flow; body surface in computation colored by pressure.

plane that, traversing from windward to leeward side, the shock becomes weaker and yields an expansion fan. Further, C2 and C3 are traces of a variable-strength, roughly cone-shaped shock, which is stronger on the windward and leeward sides, but weaker in the lateral direction. Note also the relatively localized spanwise extent of the feature denoted C4, whose genesis is described in further detail in Sec. III.F. The overall wave structure is further elucidated in Fig. 7b, which depicts the portion of isosurfaces of $\mathbf{V} \cdot \nabla p$ below the lateral plane, colored by static pressure. A layered wave structure is observed: the shock C1 extends from the windward side and ends at the lateral plane. The expansion E3 envelops the recompression shock C3, which in turn encapsulates the structure C4.

D. Flow on Afterbody

The surface oil flow represents the footprint of off-surface structures and provides an indication of the surface skin friction pattern. Figures 8a and 8c exhibit windward and side-view experimental observations [15]. For clarity, in each, the experimentalists have marked select surface streaks. The corresponding computations are plotted in Figs. 8b and 8d, respectively. For this purpose, particles are released at the first mesh point away from the surface and are then constrained to lie in the same computational plane. In addition to the surface pattern, the body is colored by static pressure. The view from the windward side, Figs. 8a and 8b, exhibits the movement of surface flow away from the windward side to the leeward side, under the influence of the pressure gradient associated with C2. The side views, Figs. 8c and 8d, show this circumferential movement, leading to an accumulation near the upper surface. Note that the boundary layer on the leeward surface, after encountering the shoulder expansion E1, experiences a mild, adverse pressure gradient. However, neither the computation nor experiment indicate separation on this surface. Similarly, despite the shock C1, the boundary layer on the windward surface does not separate. A more specific comparison between the experiment and computation is difficult because of the qualitative nature of the observation. Visual inspection suggests, however, that the experimental lines deviate to a larger extent along the circumferential direction than in the computation. However, as shown later, the main features of the off-surface flow are reproduced accurately.

Figure 9 exhibits the surface pressure along the leeward ($\phi = 180$ deg), lateral ($\phi = 90$ deg), and windward ($\phi = 0$ deg) surfaces on the three different meshes, together with the experimental values, in which errors are estimated to be 3% [15]. Note that the X coordinate is measured along the afterbody, that is, at a 10 deg angle to the freestream. The afterbody is of length $L/R = 3$, but the actual juncture, easily discernible on the windward and leeward planes by the sudden change in surface pressure, is at about $L/R = 3.75$. In each case, the computed values have therefore been translated so that the computational effect of the juncture is similar to that observed in the experiment. At each station plotted, pressure values are independent of the mesh, indicating grid-converged results. Comparing with the experiment, on the leeward side, the drop in pressure is computed accurately (Fig. 9a). As noted earlier, the sharp drop associated with E1 is followed by a gentle recovery as fluid approaches this plane from the sides. The freestream value is approximately recovered at the base. Proceeding around the periphery, on the lateral plane, $\phi = 90$ deg (Fig. 9b), the experiment

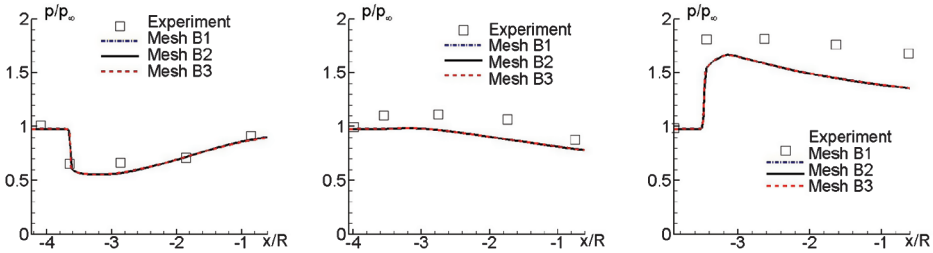

a) Leeward plane, $\phi = 180$ b) Lateral plane, $\phi = 90$ c) Windward plane, $\phi = 0$

Fig. 9 Comparison of pressure on afterbody.

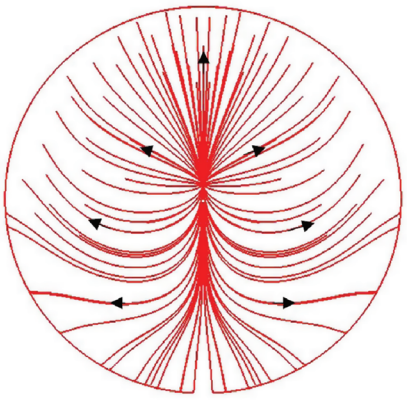

a) Restricted streamlines on base surface

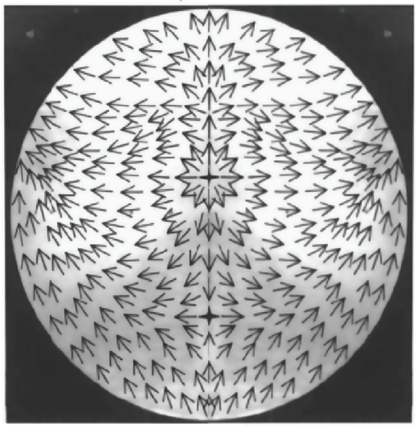

b) Experimental base streamline profiles

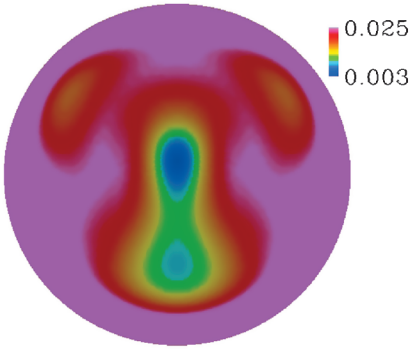

c) Skin friction pattern on base

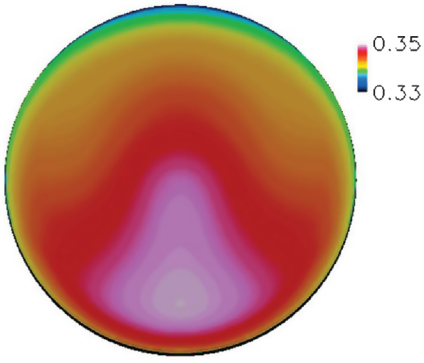

d) Base pressure contours

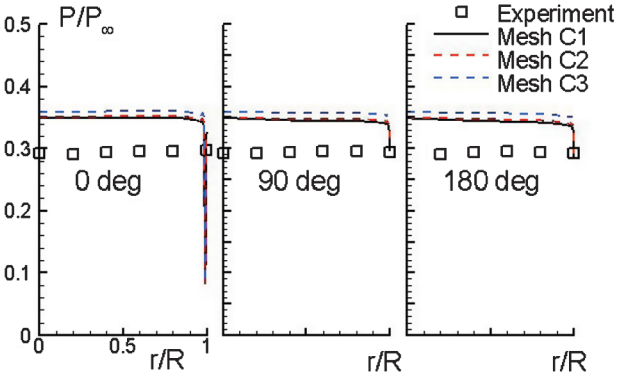

e) Base pressure comparison with data

Fig. 10 Base flow features (Fig. 10b adapted from [14] by reflecting velocity vectors about symmetry plane).

indicates a rise above the freestream value before relaxing near the base, whereas the computed value is flat initially before the decline. Over the range of the data plotted, maximum errors are about 15%. The higher pressure gradient in the experiment is consistent with the sharper turn in surface pattern observed earlier. On the windward surface, Fig. 9c, the rise in pressure associated with the shock is underpredicted by about 10%. The inviscid rise associated with a Mach 2.5 flow at a 10 deg turn angle is about 1.8, which is close to the experimentally observed value. Although the plane is one of symmetry, the spanwise relief effect gives rise to an essentially three-dimensional structure and the subsequent relief is more pronounced in the computation.

E. Structure of Flowfield on Base Surface

Figure 10 exhibits features of the flow on the flat base surface. Computed and experimental surface flow patterns are shown in Figs. 10a and 10b, respectively. (Note that, because the experimental oil flow reproduces poorly in the scanning process, the velocity vectors inferred by the experimentalists [14] have been reflected about the vertical plane.) There is generally good agreement in oil-flow direction in the upper and side regions. Both indicate the presence of a nodal point of attachment (N_1) similar to that observed for the axisymmetric case. In the computation, this occurs at $r = 0.084$ above the centerline of the base, whereas in the experiment, it is noted as occurring slightly above the center of the base. However, in the experiment, a saddle is inferred roughly midway between the node and the lower edge, leading to upward movement of fluid from the lower edge. In contrast, the computations indicate a downward movement of fluid all the way to the edge on the windward side. This discrepancy, also reflected in the inclination of the windward shear layer (shown in Fig. 14, to be discussed later) may reflect a deficiency in the RANS model in the low-speed region near the base. The effect of enhanced eddy viscosity tends to eliminate critical point pairs (see, for example, [37]). Indeed, the skin friction variation on the base, shown by computing the velocity magnitude at the first plane away

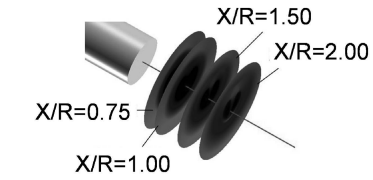

a) Schematic of planes plotted

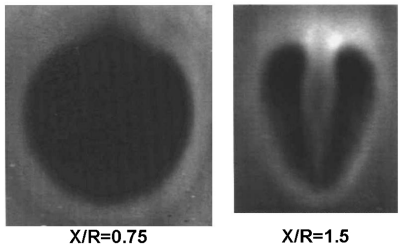

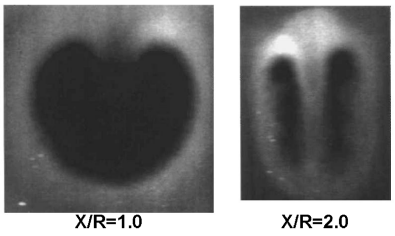

b) Experiment [15] - Mie-scattering technique

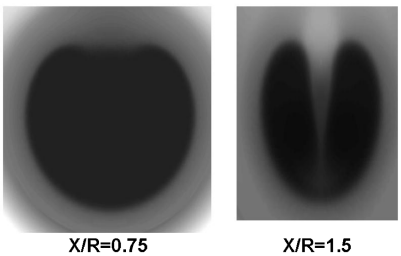

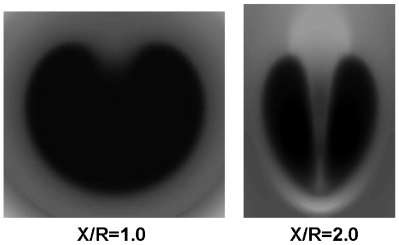

c) Computation - density variation in grayscale

Fig. 11 Comparison of mean flow structure with end-view images.

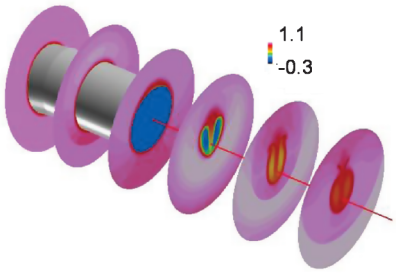

a) *u* velocity

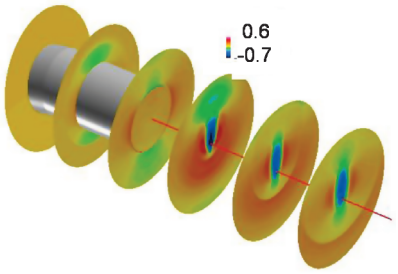

b) *v* velocity

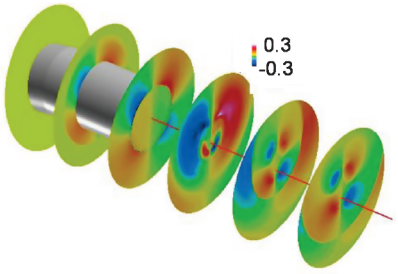

c) *w* velocity

Fig. 12 Evolution of flowfield downstream of base: velocity components.

from the base in Fig. 10, suggests a local minimum at about the location where the experimental saddle point is inferred. Ongoing simulations with a detached eddy method should help resolve the issue, though new critical points are anticipated to arise in saddle-node pairs for topological consistence. Minima in the skin friction profile are also observed in the upper regions of $\phi \sim 150$ deg. The base pressure, Fig. 10d, varies relatively little, similar to that for the axisymmetric situation [1]. Slightly higher values are obtained near the lower region as a consequence of the higher windward pressure.

Figure 10e exhibits the surface pressure at three different rays along the base, corresponding to the windward, lateral, and leeward directions. The computations show only modest change between the three meshes. Pressures on mesh C3, which is the coarsest of the three because both sides of the symmetry plane are discretized with the same number of points as mesh C1, are slightly higher. However, the more refined meshes, C1 and C2, show very similar results. Both the computation and experiment show relatively flat profiles. As noted in [15], the experimental value is about half that observed in the axisymmetric case. The computational value ($p/p_\infty \sim 0.35$) exceeds the experimental value by about 15%. Interestingly, the current RANS variant predicts a relatively flat profile, in contrast to the observations of Forsythe et al. [6], who observed much greater variations with several other RANS models and recovered a flat profile only with detached eddy simulations.

F. Comparison with Experimental End-View Flow Visualization

The discussion of the off-surface flow in the base region is initiated by comparing end-view averaged Mie-scattering experimental flow images with the computation (visualized with the grayscale density) as shown in Fig. 11. Four planes downstream of the base are visualized as shown schematically in Fig. 11a; note that the planes are normal to the axis of the afterbody (as opposed to the freestream direction). The agreement between the experiment and computation, in terms of the dominant features, is clearly evident. At the first station plotted, $X/R = 0.75$, the dark region is roughly circular except for the leeward side, where a slight depression is visible. Proceeding downstream, the depression penetrates downward until two clear lobes are observed. These vertically aligned structures are separated by a septum, which grows downward. The connection between the lobes in the lower region is associated with C4 in Figs. 5 and 6, since traversing vertically downward along the symmetry plane, a feature may be inferred with a change in hue observed in the experiment. In the last station plotted, the experiment indicates near-complete lobe separation, whereas in the computation a small connecting region is evident. Extensive analysis of the computation indicates that some features are delayed in the computation; note that the computed pattern at $X/R = 2$ more closely resembles the experiment at $X/R = 1.5$. In each figure, the lighter regions around

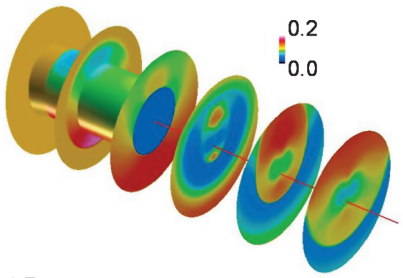

a) Pressure

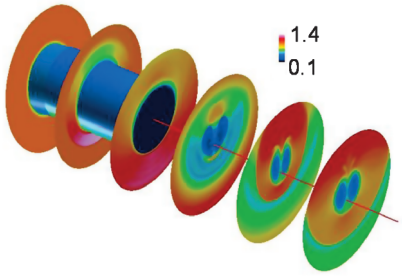

b) Density

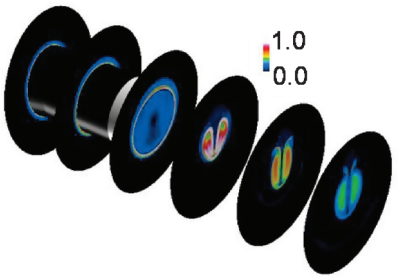

c) Vorticity

Fig. 13 Evolution of flowfield downstream of base: thermodynamic quantities and vorticity magnitude.

the outer periphery of the dark lobes, representing higher velocity fluid from the outer part of the afterbody boundary layer, are also evident.

The evolution of the lobed mean structures in the computation and experiment is explored by examining several variables in Figs. 12 and 13, which plot the velocity components, pressure, density, and vorticity magnitude at several planes far downstream of the experimental observation region. The streamwise velocity (Fig. 12a) shows a pattern similar to that in the experimental images. The lobes are observed to be low streamwise velocity features. Proceeding downstream, the effect of entrainment is to gradually equalize the velocity over the cross-sectional plane. Figure 12b shows that the septum region is characterized by negative vertical velocities, indicating gross movement of fluid from the leeward to the windward side, with velocities reaching as high as 70% of the freestream velocity. Spanwise velocities show the entrainment of the outer flow toward the axis. However, just beneath the axis, the situation is reversed, and fluid moves outward. The shear layer between the entrained and external fluid is most clearly visible in this figure. The pressure field (Fig. 13a) is consistent with the wave structure described in Fig. 7. Note the small region of high pressure just beneath the axis, which corresponds to the structure denoted earlier as C4. The low-pressure core extends in size, even as the pressure value recovers. At the last station, the recompression shock is clearly visible, but other features gradually become less distinct. Density contours in Fig. 13b show that the cores are also lower-density regions. Furthermore, near the end of the domain, the interaction of the two vortical structures yields slip surfaces appearing as narrow strands on the upper edges of the lobes. Vorticity contours in Fig. 13c show that the low-velocity, low-pressure, and low-density lobes are also characterized by high values of vorticity. Details of the vector vorticity field are presented in Sec. III.H.

G. Velocity Field in Base Region

A kinematic description of the flowfield in the immediate vicinity of the base region is obtained by examining velocity vectors on the symmetry and lateral planes. Figure 14 compares experimentally inferred velocity vectors with computational results on the symmetry plane. Note that the coordinate system is as shown in Fig. 2, that is, with the X axis inclined at 10 deg to the horizontal. Figure 14a represents a wider view, whereas Fig. 14b exhibits a zoomed-in view. Although the plotting density of the vectors and their lengths have not been matched with those in the experiment (a more quantitative assessment is provided later in Fig. 15), the broad agreement is evident. The "recirculation region" downstream of the base is roughly triangular in shape, with the apex below the axis. Although there is qualitative agreement in the broad features, it is apparent that the shear layer formed downstream by the fluid emanating from the windward side is almost horizontal (parallel to the axis) in the computation, but is inclined upward in the experiment. The experimental evidence suggests the existence of two stagnation points marked by the stars in Fig. 14b. To detect stagnation points in the simulation, and to provide insight into the topological structure of the flow on the symmetry plane, Fig. 14c plots restricted streamlines on the symmetry plane. The streamline pattern is described in terms of critical points, which may be distinguished into nodal and saddle points (see [38–40] for a discussion of critical points). By convention, points that occur on the boundary are denoted as half-points (indicated by primes). Thus, the pattern exhibits three half-saddles: S_1', S_2', and S_3'. Two (spiral) nodes are observed in the flow, N_1 and N_2, together with a saddle point, S_4. The node N_1 is unstable in the sense that the fluid moves away from it (source, or fluid entering the symmetry plane), whereas N_2 is stable for the opposite reason (sink, or fluid leaving the symmetry plane). Topologically, this pattern is identical to that shown for the axisymmetric case (Fig. 1), in which the two nodes are replaced by "centers" in the axisymmetric situation, and the saddle is marked wake stagnation point. Interestingly, the evolution of the pattern from that in Fig. 1 to that in Fig. 14c is closely related to that described in the context of unsteady bifurcations occurring when the Reynolds number is increased in the flow past an axisymmetric body at a zero angle of attack [41]. This comparison will be elucidated further in the context of the discussion on the vorticity field below.

The streamline pattern observed in Fig. 14c is consistent with the experimental observation of an "inverted-S" pattern [14]. This follows from the fact that a streamline traversing from N_1 to N_2 forms an laterally inverted-S pattern. Because the crossflow velocity is zero on the symmetry plane, N_1, N_2, and S_4 are each stagnation points. In contrast to the experiment, which postulates the existence of two stagnation points, three are observed in the computation. The upper point, N_1, occurs at $X = 0.55$, $Y = 0.52$, which is close to the experimental value of $X = 0.55$, $Y = 0.45$ (a five-point star in the experimental result). The lower node occurs at (1.14, −0.412), while the saddle S_4 occurs at (1.39, −0.33). The experimental value (1.2, −0.3), a four-point star in the experimental result, corresponds closely to N_2. Note that the rules governing the numbers and types of critical points is satisfied in the computation; the number of saddles exceeds that of nodes by one-half, which is the number in an equivalent subregion of an unseparated flow.

A more quantitative assessment of the flowfield on the symmetry plane is shown in Fig. 15, in which the color scheme for the computation and experiment differ slightly from each other. Also, the error in the experimental observations for velocities normalized by the freestream velocity is noted to be less than 2% for these quantities. The X velocity (Fig. 15a and 15c) and Mach contours (Fig. 15b and 15d) exhibit similar low-speed, roughly triangular regions. Overall, the variable ranges are in reasonable agreement: on the leeward side, the expansion associated with the shoulder yields peak values approaching 10% above the freestream velocity in each, and peak Mach numbers reach about 3.2. The rate at which the shear layer expands is considerably larger for the leeward as opposed to the windward side, a point noted in the experiment as well. However, some differences in the details are evident. One aspect, noted earlier

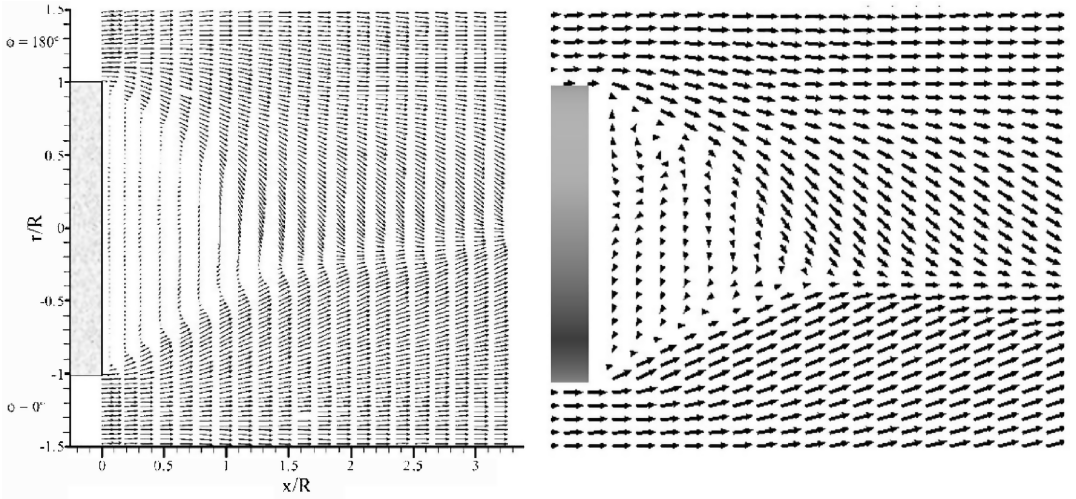

a) Overall view. Left: Experiment, Right: Computation

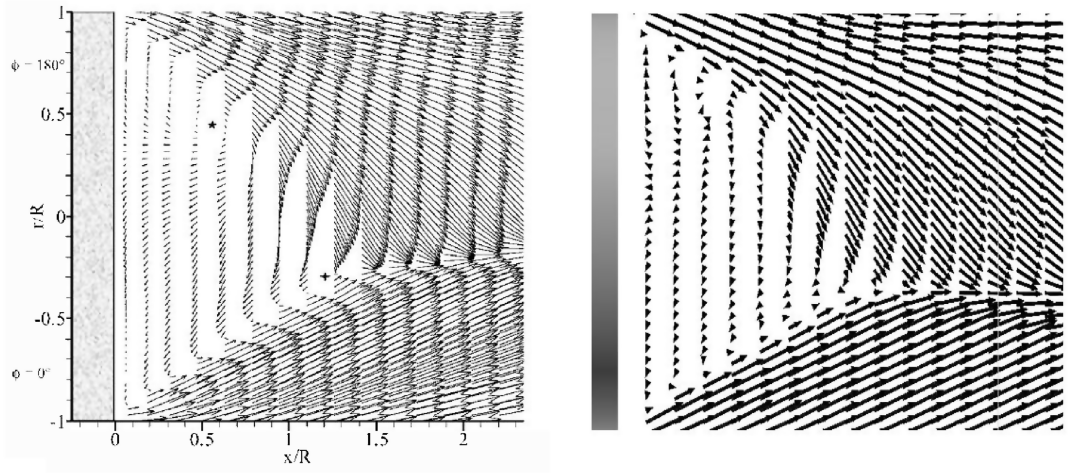

b) Zoomed view. Left: Experiment, Right: Computation

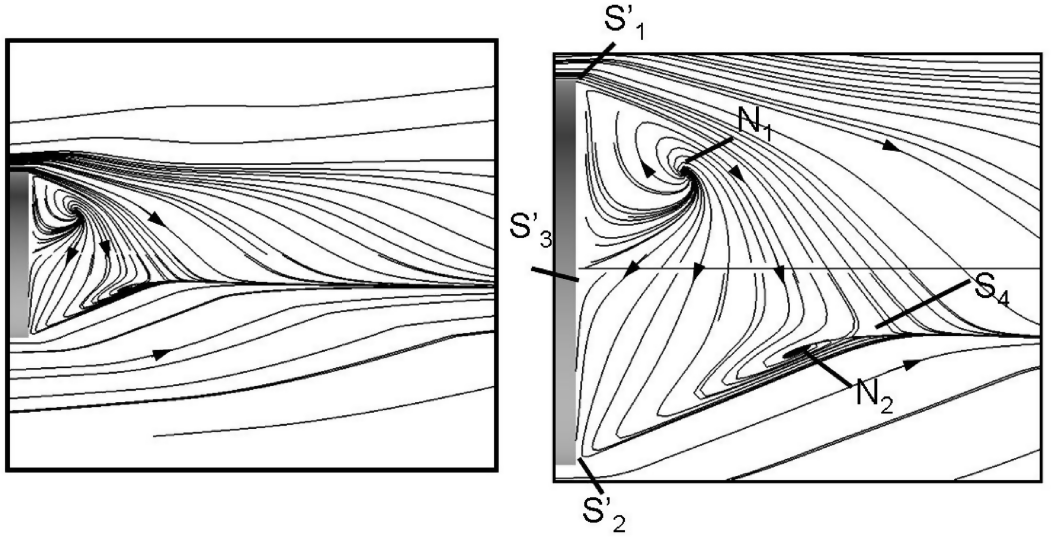

c) Symmetry plane streamlines (computed)

Fig. 14 Velocity field on symmetry plane.

in the context of the velocity vectors, is the inclination of the shear layer developing from the windward shoulder. Some trends appear contradictory: relative to the computations, the experiments indicate faster recovery than the computation for velocity, but slower for the Mach number.

A comparison of the measured and computed velocity vectors in the lateral plane is presented in Fig. 16. Again, the velocity vectors are meant to provide a broad comparison between the two approaches. Because the flow is symmetric about the vertical plane, only one side of the base is plotted in Figs. 16a and 16b. In each case,

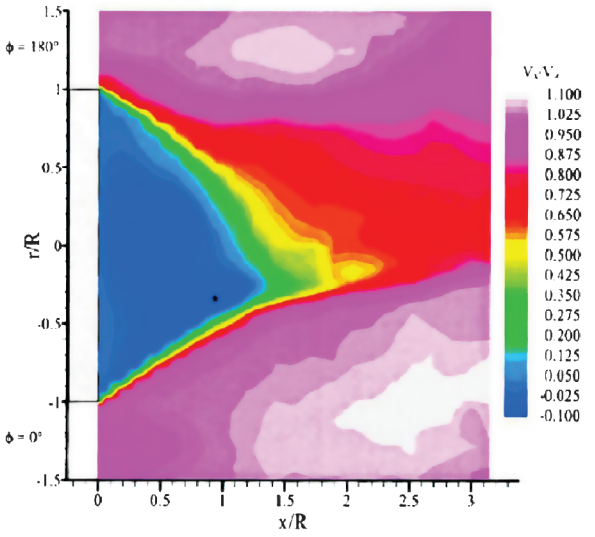

a) U_x Experiment [14]

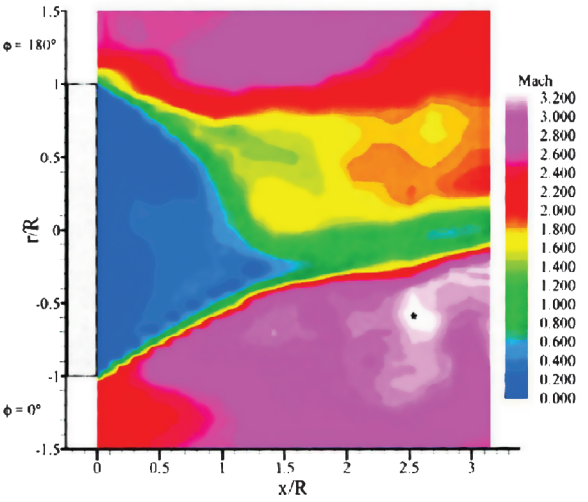

b) Mach number. Experiment [14]

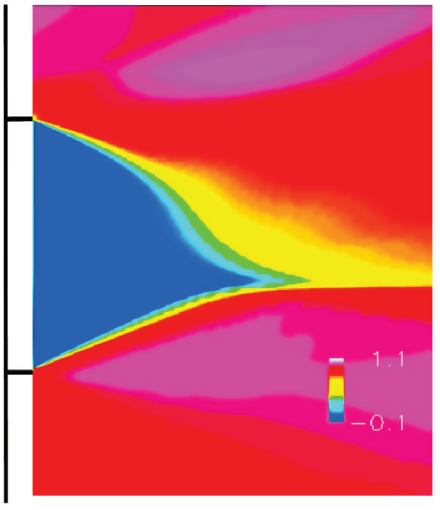

c) U_x Computation

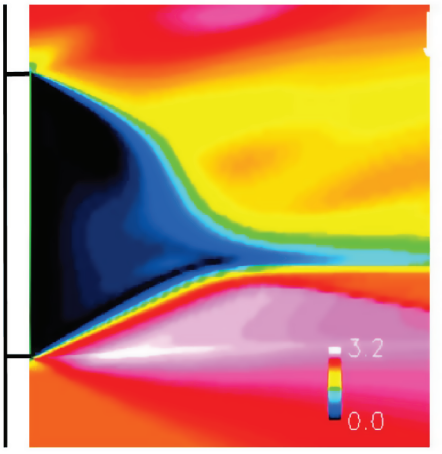

d) Mach number Computation

Fig. 15 Velocity and Mach number contours on symmetry plane.

velocity vectors along the centerline are seen to accelerate beyond a certain distance away from the base. This yields a jetlike structure at the symmetry plane. Thus, the velocity is large in the far field, and as the symmetry plane is approached, the velocity first diminishes and then increases again. Restricted streamlines are shown in Fig. 16c. Topologically, the situation is similar to the symmetry plane counterparts shown earlier in Fig. 14c; corresponding critical points have been marked. However, in this case the saddle point occurs upstream of the nodal points. Furthermore, both nodal points are unstable; this represents a net movement of fluid through the plane from the leeward to the windward side, as is consistent with the downward movement of fluid on the symmetry plane (Fig. 14).

H. Flowfield Model

The simulations are now employed to explore the overall structure of the flow. To this end, streamlines are released on the periphery of the base. The main features are shown in Fig. 17, in which each streamline is colored by static pressure. The dominant features are two streamwise aligned vortex structures, in vast contrast to the field observed in the simpler mean flow in the axisymmetric case. Viewing downstream, the right structure is counterclockwise, consistent with each of the previous computational and experimental observations. For example, the lobes of Fig. 11 are evidently the cores of the two longitudinal structures. Similarly, the higher-speed fluid observed near the axis in Fig. 16 arises from the entrainment of fluid, as was also noted by the experimentalists.

It should be mentioned that similar structures have been observed in other base flows; for example, in [21], the incompressible flow past a cylinder was shown to yield a dual vortex flow. Another example is discussed in [41], in which the evolution of the flowfield past a sphere under increasing Reynolds number variation has been shown to yield similar longitudinal vortices. Dallmann et al. [41] also discussed the bifurcations that lead from the topological structure of Fig. 1 to that of Fig. 14 (albeit with the regular *S* instead of the inverted *S*, with fluid movement from the lower to upper spiral node).

Further analysis of the kinematic structure is performed by identifying the origin of fluid in the vortical structures. Different regimes emanating from various points on the periphery are presented in Fig. 18. Figures 18a–18d depict velocity-magnitude-colored traces of particles released at different heights in the incoming leeward-side boundary layer. The dominant part of the low-speed region immediately downstream of the base is composed of fluid emanating from the near vicinity of the leeward surface. This fluid experiences several turns, first downward, then backward toward the base surface, and outward toward the periphery of the base, forming a shear layer with the lateral, windward, and leeward boundary layers before being vented downstream. Note that the

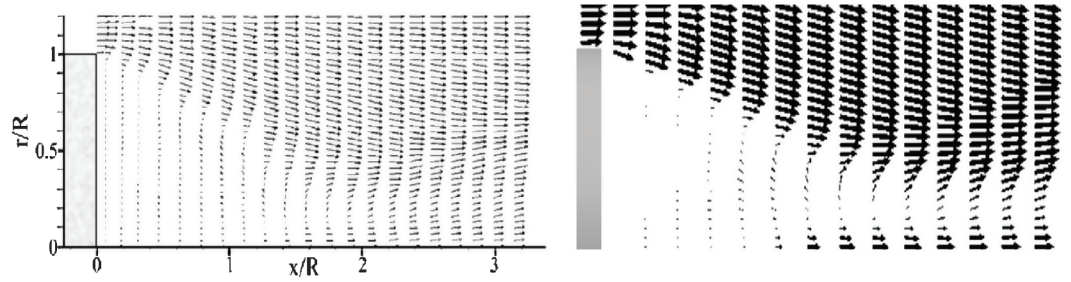

a) Overall view. Left: Experiment, Right: Computation

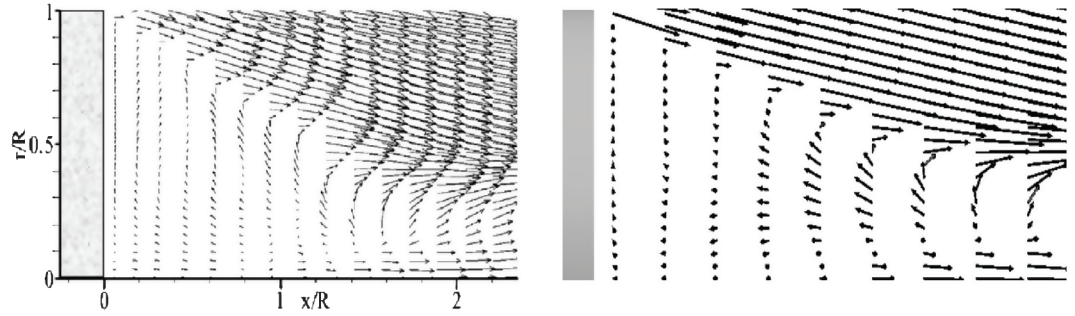

b) Zoomed view. Left: Experiment, Right: Computation

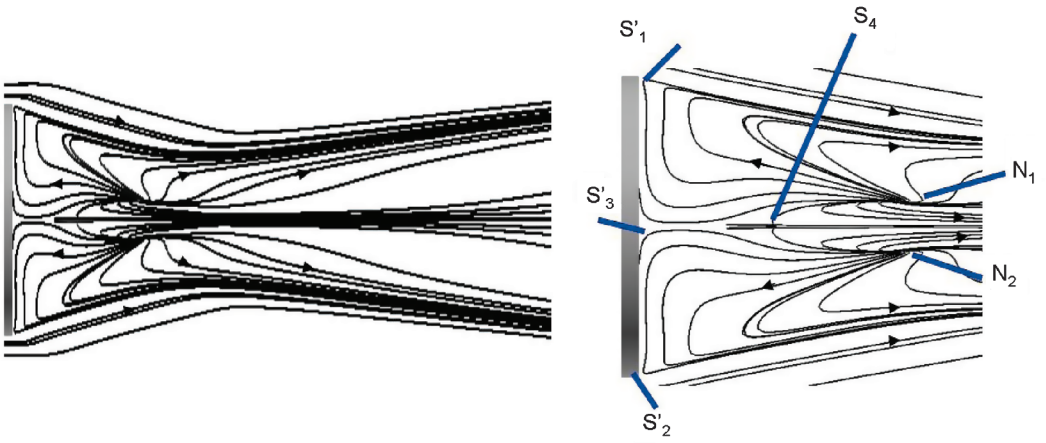

c) Restricted lateral plane streamlines (computed)

Fig. 16 Velocity field on lateral plane.

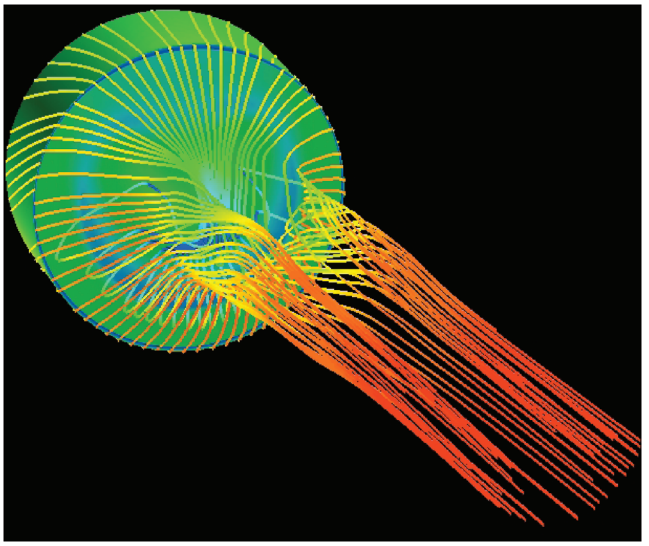

Fig. 17 Overview of flowfield structure with surface streamlines colored with pressure.

structure is open, with no permanent circulating fluid; such bubbles or dead air regions are highly unstable and do not typically occur in three-dimensional flows, even in the mean sense. Fluid from higher in the lee-side boundary layer is initially swept downstream and toward the windward side, generating the septum observed earlier, and is then entrained into the vortical structure. Fluid is released at different locations on the lateral part of the base wrap around the vortical structure as well (Figs. 18e and 18f), forming the main portion of the septum far downstream. Fluid from the windward side (Figs. 18g and 18h) essentially forms the lower envelope of the vortical structures.

The vorticity field is shown in Fig. 19, with select vortex lines colored by the x component of vorticity. On the afterbody, vortex lines A and B are circumferential, traversing counterclockwise when viewed in the downstream direction, and are slightly forward inclined relative to the cross-sectional plane. In the base region, the outer structure remains similar (C). However, vortex lines traversing the low-velocity region are continuous and indicate the existence of a horseshoelike structure; this is consistent with the absence of spiral nodes on the base surface (Fig. 10). The two lobes observed earlier may therefore be viewed as two legs of the same structure. Vortex lines D, E, and F thus traverse upstream (negative ω_x) in the right lobe (again looking downstream) and downstream in the left lobe. The mean vorticity field in the three-dimensional situation is vastly

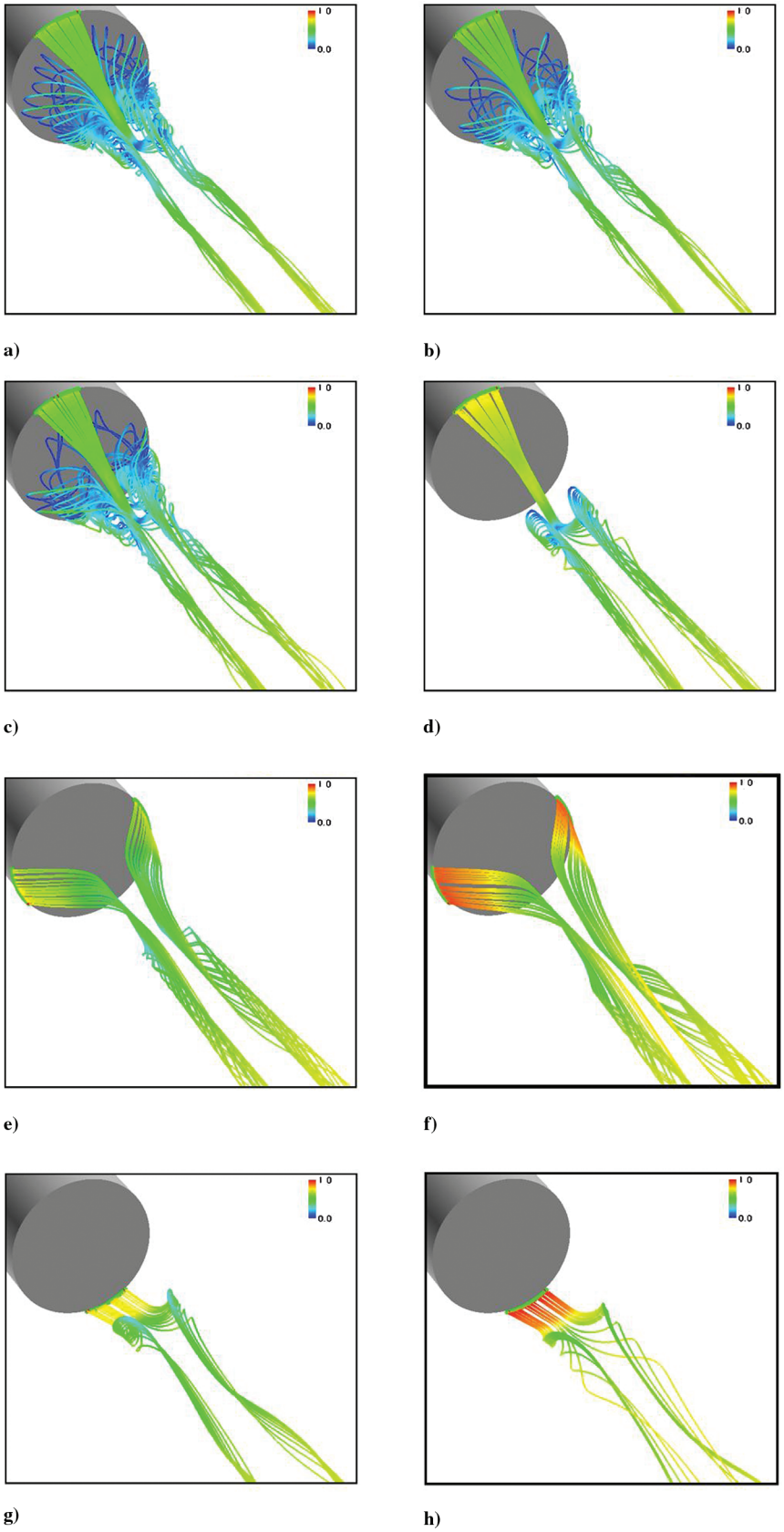

Fig. 18 Regimes generated by releasing traces at different locations around periphery of base. Radial distances (r/δ) from the afterbody surface: a) 0.001, b) 0.005, c) 0.025, d) 0.05, e) 0.001, f) 0.2, g) 0.001, and h) 0.2.

different from the axisymmetric pattern implicit in Fig. 1. In that case, vortex lines remain essentially circumferential closed loops. This evolution of circumferential vortex lines into a horseshoe-type structure has been discussed in the context of the instability and bifurcations in the former under Reynolds number variation in incompressible axisymmetric flows [41]. In this sense, the effect of the third dimension corresponds to the time axis in the axisymmetric situation.

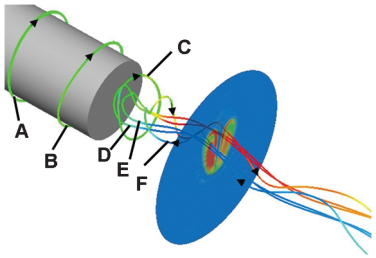

Fig. 19 Vortex lines colored with x component of vorticity. Crossflow plane shows vorticity magnitude.

IV. Conclusions

The three dimensionality introduced in the base region of flow past a cylindrical afterbody inclined at a 10 deg angle of attack is examined numerically. The motivation stems from experimental observations that show that the base pressure is reduced to about half that in the axisymmetric case. This has obvious implications on base drag, which is already a major component of total drag at supersonic speeds. The mean compressible three-dimensional Reynolds-averaged Navier–Stokes equations are employed with an advanced k–ϵ turbulence model, including a correction for compressibility that is crucial in the free shear layer development downstream of the body. The equations are solved with a third-order upwind biased method, together with a nondiffusive limiter. The specific configuration considered mimics experiments reported in the literature, which have yielded an extensive set of high-fidelity qualitative and quantitative data, including surface oil flow, side- and end-view Mie scattering, and schlieren images and surface pressures on the afterbody and base. Comparisons of numerical and experimental results for the mean flow indicate that the main coherent features in the experiment are reproduced accurately with some modest differences in the location and inclination of some features. Quantitative differences between the computation and experiment are characterized by examining surface pressures (mesh-resolved simulations suggest errors of about 15%); these baseline evaluations serve to guide ongoing detached eddy simulations. Based on satisfactorily accurate mean flow feature reproduction, the computations are employed to develop a comprehensive flowfield model. Stream traces are employed to demonstrate the generation of two longitudinally aligned vortical structures, for which the traces are observed in experimental and computational end-view images: the right structure looking downstream has a counterclockwise orientation, whereas the left structure is its mirror image. The wave structure observed in the computation and experiment is resolved and correlated to the streamline structure. It is shown that, in the mean sense, the near-wall leeward fluid entering the base region accounts for much of the low-speed fluid in the base, as well as in the cores of the vortical structures. Fluid originating higher in the leeward boundary layer and on the lateral edges is entrained near the symmetry plane, whereas the windward shear layer forms a lower envelope of the fluid disturbed by the body. The evolution is compared to unsteady axisymmetric situations and is discussed in the context of vorticity redistribution in the base region. Future work will focus on examining shear layer unsteadiness with detached eddy simulations and on exploring control strategies that exploit this understanding of the mean flow.

Acknowledgments

The author is grateful to Craig Dutton and William Oberkampf for providing permission to reprint portions of their work. This work was supported by the U.S. Air Force Office of Scientific Research (Monitors: John Schmisseur and Fariba Fahroo). Computational resources were made available by the Major Shared Resource Centers at the Aeronautical Systems Center, the U.S. Army High Performance Computing Research Center, and the U.S. Naval Oceanographic Office.

References

[1] Lamb, J., and Oberkampf, W., "Review and Development of Base Pressure and Base Heating Correlations in Supersonic Flow," *Journal of Spacecraft and Rockets*, Vol. 32, No. 1, Jan.–Feb. 1995, pp. 8–23. doi:10.2514/3.26569

[2] Slucomb, T., "Project Fire II Afterbody Temperatures and Pressures at 11.35 Kilometers per Second," NASA TM X-1319, 1966.

[3] Herrin, J., and Dutton, J., "Supersonic Base Flow Experiments in the Near Wake of a Cylindrical Afterbody," *AIAA Journal*, Vol. 32, No. 1, 1994, pp. 77–83. doi:10.2514/3.11953

[4] Herrin, J., and Dutton, J., "Supersonic Near-Wake Afterbody Boattailing Effects on Axisymmetric Bodies," *Journal of Spacecraft and Rockets*, Vol. 31, No. 6, 1994, pp. 1021–1028. doi:10.2514/3.26553

[5] Bourdon, C., and Dutton, J., "Planar Visualizations of Large-Scale Turbulent Structures in Axisymmetric Supersonic Separated Flows," *Physics of Fluids*, Vol. 11, No. 1, 1999, pp. 201–213. doi:10.1063/1.869913

[6] Forsythe, J., Hoffmann, K., and Squires, K., "Detached-Eddy Simulation with Compressibility Corrections Applied to a Supersonic Axisymmetric Base Flow," AIAA Paper 2002-0586, Jan. 2002.

[7] Baurle, R., Tam, C.-J., Edwards, J., and Hassan, H., "Hybrid Simulation Approach for Cavity Flows: Blending, Algorithm, and Boundary Treatment Issues," *AIAA Journal*, Vol. 41, No. 8, Aug. 2003, pp. 1463–1480. doi:10.2514/2.2129

[8] de Feo, D., and Shaw, S., "Turbulence Modeling and Supersonic Base Flows," AIAA Paper 2007-1083, Jan. 2007.

[9] Barnhardt, M., Drayna, T., Nompelis, I., Candler, G., and Garrard, W., "Detached Eddy Simulations of the MSL Parachute at Supersonic Conditions," AIAA Paper 2007-2529, 2007.

[10] Sinha, K., "Effect of Reynolds Number on Detached Eddy Simulation of Hypersonic Base Flow," AIAA Paper 2007-1457, 2007.

[11] Sinha, K., and Reddy, S., "Hypersonic Turbulent Reacting Flow Simulation of Fire II Re-Entry Vehicle," AIAA Paper 2007-805, 2007.

[12] Kawai, S., and Fujii, K., "Time-Series and Time-Averaged Characteristics of Subsonic to Supersonic Base Flows," *AIAA Journal*, Vol. 45, No. 1, Jan. 2007, pp. 289–301. doi:10.2514/1.24601

[13] Oberkampf, W., and Bartel, T., "Symmetric Body Vortex Wake Characteristics in Supersonic Flow," *AIAA Journal*, Vol. 18, No. 11, 1980, pp. 1289–1297. doi:10.2514/3.50884

[14] Boswell, B., and Dutton, J., "Velocity Measurements in a Three-Dimensional Compressible Base Flow," *AIAA Journal*, Vol. 41, No. 5, May 2003, pp. 785–794. doi:10.2514/2.2040

[15] Boswell, B., and Dutton, J., "Flow Visualizations and Measurements of a Three-Dimensional Supersonic Separated Flow," *AIAA Journal*, Vol. 39, No. 1, Jan. 2001, pp. 113–121. doi:10.2514/2.1277

[16] Kastengren, A., and Dutton, J., "Large-Structure Topology in a Three-Dimensional Supersonic Base Flow," *AIAA Journal*, Vol. 43, No. 5, May 2005, pp. 1053–1063. doi:10.2514/1.10717

[17] Murman, S., and Aftosmis, M., "Dynamic Analysis of Atmospheric-Entry Probes and Capsules," AIAA Paper 2007-0074, 2007.

[18] Sahu, J., "Unsteady Flow Computations of a Finned Body in Supersonic Flight," AIAA Paper 2007-3933, 2007.

[19] Sahu, J., "Three-Dimensional Base-Flow Calculation for a Projectile at Transonic Velocity," *AIAA Journal*, Vol. 27, No. 2, 1989, pp. 138–139. doi:10.2514/3.10074

[20] Sahu, J., "Three-Dimensional Flow Calculations for a Projectile with Standard and Dome Bases," *Journal of Spacecraft and Rockets*, Vol. 31, No. 1, 1994, pp. 106–111. doi:10.2514/3.26409

[21] Himeno, R., Shiryama, S., Kamo, K., and Kuwahara, K., "Computational Study of Three-Dimensional Wake Structure," AIAA Paper 85-1617, 1985.

[22] Knight, D., and Degrez, G., "ShockWave Boundary Layer Interactions in High Mach Number Flows—A Critical Survey of Current CFD Prediction Capabilities," AGARD Tech. Rept. AR-319, Vol. 2, 1997.

[23] Gaitonde, D., Shang, J., Garrison, T., Zheltovodov, A., and Maksimov, A., "Three-Dimensional Turbulent Interactions Caused by Asymmetric Crossing-Shock Configurations," *AIAA Journal*, Vol. 37, No. 12, 1999, pp. 1602–1608.

doi:10.2514/2.660
[24] Gaitonde, D., Shang, J., and Edwards, J., "Structure of a Supersonic Three-Dimensional Cylinder/Offset-Flare Turbulent Interaction," *Journal of Spacecraft and Rockets*, Vol. 34, No. 3, 1997, pp. 294–302. doi:10.2514/2.3232
[25] Gaitonde, D., "Mean Flowfield Structure of a Supersonic Three-Dimensional Base Flow," AIAA Paper 2008-573, 2008.
[26] Pulliam, T., and Chaussee, D., "A Diagonal Form of an Implicit Approximate-Factorization Algorithm," *Journal of Computational Physics*, Vol. 39, No. 2, 1981, pp. 347–363. doi:10.1016/0021-9991(81)90156-X
[27] Launder, B., and Sharma, B. I., "Application of the Energy Dissipation Model of Turbulence to the Calculation of Flows near a Spinning Disk," *Letters in Heat and Mass Transfer*, Vol. 1, 1974, pp. 131–138. doi:10.1016/0094-4548(74)90150-7
[28] Sarkar, S., Erlebacher, G., Hussaini, M., and Kreiss, H., "The Analysis and Modelling of Dilational Terms in Compressible Turbulence," *Journal of Fluid Mechanics*, Vol. 227, 1991, pp. 473–493. doi:10.1017/S0022112091000204
[29] Rizzetta, D., "Numerical Simulation of Vortex Induced Oblique Shock-Wave Distortion," AIAA Paper 96-0039, Jan. 1996.
[30] Roe, P., "Approximate Riemann Solvers, Parameter Vectors and Difference Schemes," *Journal of Computational Physics*, Vol. 43, 1981, pp. 357–372. doi:10.1016/0021-9991(81)90128-5
[31] van Leer, B., "Flux-Vector Splitting For the Euler Equations," Inst. for Computer Applications in Science Tech. Rept. 82-30, Sept. 1982.
[32] van Albada, G., van Leer, B., and Roberts, W., "A Comparative Study of Computational Methods in Cosmic Gas Dynamics," *Astronomy and Astrophysics*, Vol. 108, 1982, pp. 76–84.
[33] Beam, R., and Warming, R., "An Implicit Factored Scheme for the Compressible Navier–Stokes Equations," *AIAA Journal*, Vol. 16, No. 4, 1978, pp. 393–402. doi:10.2514/3.60901
[34] Visbal, M., and Gordnier, R., "A High-Order Flow Solver for Deforming and Moving Meshes," AIAA Paper 2000-2619, June 2000.
[35] Sun, C., and Childs, M., "A Modified Wall Wake Velocity Profile for Turbulent Compressible Boundary Layers," *Journal of Aircraft*, Vol. 10, No. 6, 1973, pp. 381–383. doi:10.2514/3.44376
[36] Blazek, J., *Computational Fluid Dynamics*, Elsevier Science, New York/Amsterdam, 2001.
[37] Gaitonde, D., Visbal, M., Shang, J., Zheltovodov, A., and Maksimov, A., "Parametric Investigation of Flowfield Structure and Validation Issues in 3-D Crossing-Shock Wave/Turbulent Boundary Layer Interactions," *Int. Conf. on Methods of Aerophysical Research*, Inst. of Theoretical and Applied Mechanics, Novosibirsk, Russia, June–July 1998, pp. 328–335.
[38] Tobak, M., and Peake, D., "Topology of Three-Dimensional Separated Flows," *Annual Review of Fluid Mechanics*, Vol. 14, 1982, pp. 61–85. doi:10.1146/annurev.fl.14.010182.000425
[39] Chapman, G., and Yates, L., "Topology of Flow Separation on Three-Dimensional Bodies," *Applied Mechanics Reviews*, Vol. 44, No. 7, July 1991, pp. 329–345. doi:10.1115/1.3119507
[40] Dallmann, U., "Topological Structures of Three-Dimensional Vortex Flow Separation," AIAA Paper 83-1735, 1983.
[41] Dallmann, U., Hilgenstock, A., Riedelbauch, S., Schulte-Werning, B., and Vollmers, H., "On the Footprints of Three-Dimensional Separated Vortex Flows Around Blunt Bodies," CP-494, AGARD, Neuilly-sur-Seine, France, 1991, pp. 9-1–9-13.